Elastic scattering of 65 MeV polarized protons

H. Sakaguchi, M. Nakamura, K. Hatanaka,* A. Goto,†
T. Noro,* F. Ohtani, H. Sakamoto, H. Ogawa, and S. Kobayashi
Department of Physics, Kyoto University, Kyoto 606, Japan
(Received 3 March 1982)

Elastic scattering of 65 MeV polarized protons from 25 nuclei (^{16}O–^{209}Bi) has been measured. The volume integral of the real central part of the optical potential (J_R) shows a behavior similar to the binding energy curve for the target mass number. The mean square radius of the real central part of the optical potential is found to obey the relation $\langle r^2\rangle_{\rm pot}=(0.937\pm0.012)A^{2/3}+(6.42\pm0.21)$ fm^2. By comparing with the systematics of the charge distributions obtained from electron scattering data, it is found that the effective two-body interaction range between an incident proton and a nucleon in the target has a target mass number dependence given by $\langle r^2\rangle_{\rm int}=(0.132\pm0.013)A^{2/3}+(4.24\pm0.24)$ fm^2. Assuming this relation, root mean square radii of the point nucleon distributions are obtained. The dependences of the J_R value and the $\langle r^2\rangle_{\rm pot}$ value on the mass number and energy obtained here are compared critically with recent microscopic optical potential calculations.

NUCLEAR REACTIONS ^{16}O, ^{24}Mg, ^{28}Si, ^{40}Ar, ^{40,44,48}Ca, ^{46,48,50}Ti, ^{54,56}Fe, ^{58,60,62,64}Ni, ^{89}Y, ^{90}Zr, ^{98,100}Mo, ^{144}Sm, ^{208}Pb, ^{209}Bi($\vec{p}$,p), $E=65$ MeV; measured $\sigma(\theta)$, $A(\theta)$; deduced optical-model parameters, mean-square nuclear radii, and volume integrals for the real central potential.

I. INTRODUCTION

Recent progress in nuclear matter theory has made it possible to understand the nuclear optical potential microscopically in terms of a two-body nucleon-nucleon interaction. Jeukenne, Lejeune, and Mahaux (JLM)[1–4] at Liege and Brieva and Rook[5–9] (BR) at Oxford have calculated the nuclear optical potential microscopically. In order to check critically these global optical potential theories and to extract new aspects in many body problems, it is necessary to measure accurately proton elastic scattering over a wide range of target nuclei and over a wide range of energies relative to the Fermi energy. In applying nuclear matter theory to scattering problems there are many difficulties to overcome by using suitable approximations. The most ambiguous process among them is the transformation procedure from infinite nuclear matter to finite nuclei, such as the process using the local density approximation (LDA). As was already pointed out by Wong[10] and Negele,[11] the LDA is not accurate in the nuclear surface region. On the other hand, the nuclear surface is the region most sensitively explored by nuclear scattering, and surface effects will be exemplified by their mass number dependence. In order to clarify the role of the nuclear surface and to check the approximation used in the theory, it is important to determine accurately the mass number dependence of the optical potential. For the LDA the energy dependence of the t matrix in nuclear matter is reflected directly in the potential depth. But in the folding potential of Brieva and Rook the situation is not so straightforward as in the LDA. For checking the validity of their approximation, the energy dependence of the optical potential will be a useful guide.

On the experimental side, the study of the optical potential has progressed after Becchetti and Greenlees's[12] work. If we plot the data available on elastic scattering in a two dimensional plane of incident proton energy versus target mass number, we notice that data are concentrated at energies below 35 MeV and for targets near magic nuclei. In addition, systematic experimental studies on the optical potential using a polarized proton beam are still scarce. Recently Fabrici *et al.* reported[13,14] measurements of the elastic scattering at several proton energies between 20 and 45 MeV. Although their systematic analysis utilized polarization data only

partially, it has clarified the energy dependence in that energy region. In the intermediate energy region, a group at Indiana University is investigating[15–17] the systematics of the optical potential in a relativistic framework. In this paper we report systematic measurements on elastic scattering of polarized protons and an analysis of data over a wide range of target mass numbers, from ^{16}O to ^{209}Bi, at an incident energy of 65 MeV. Partial results have been published.[18–20] The use of high-purity germanium (HP-Ge) detectors has made possible rapid data acquisition at this energy. The 65 MeV data are thought to be valuable not only because they fill a gap in experimental data but also because of the simplicity of the reaction mechanism; they are relatively free from the giant resonance effects and the multistep processes observed in the lower energy region. Section II describes the experimental method. In Sec. III, the method of data reduction and the error estimation are discussed. Section IV is devoted to the optical potential fitting procedure. Section V discusses systematics of the mean square radius extracted from the optical potential parameters. A comparison between experimentally obtained $\langle r^2 \rangle_{\text{pot}}$ values and microscopic calculations is presented in Sec. VI. Section VII describes the method to extract nuclear matter radii as an application of Sec. V and compares them with the 800 MeV LAMPF data. Systematics observed in the volume integral of the real central part of the optical potential is treated in Sec. VIII, together with the JLM microscopic optical potential. Conclusions and a summary are presented in Sec. IX.

II. EXPERIMENTAL METHOD

The polarized proton beam (of 10 keV energy) from the atomic beam type polarized ion source[21] (PIS) is injected axially into the Research Center for Nuclear Physics (RCNP) (Osaka University) AVF cyclotron.[22] A beam buncher in the injection system intensifies the pulsed beam peak current by about a factor of 3. The extracted beam of 65 MeV was energy analyzed and transported to the polarization experiment area.[23] As shown in Fig. 1, the beam was first focused on a target to a beam spot size of about 1×2 mm^2. After passing through the target, the polarized beam was again focused on a polarimeter target foil and then collected by a Faraday cup located downstream of the polarimeter. The beam current was monitored by a current digitizer whose output pulses were routed by a spin controller,[24] depending on the beam polarization direction.

Scattered protons were detected by 1.5 cm thick HP-Ge detectors, which were located at symmetric scattering angles to the left and right of the beam on goniometers outside the scattering chamber. In the angle region of rapidly changing angular distributions, the detectors were placed at a distance of more than 30 cm from the scattering chamber (of 26.6 cm diameter) to obtain better angular resolution. A vacuum bag was inserted between the scattering chamber and the HP-Ge cryostat to reduce the energy loss and range straggling of the scattered particles in air. For solid targets, the acceptance solid angles of the detector were 0.145 msr at forward angles ($\theta \leq 32.5°$) and 0.690 msr at backward angles ($\theta \geq 32.5°$). For gas targets, the vacuum bag was inserted between the front and back slits of a double-slit collimator. The gas target G factors of the slit system were 1.09×10^{-4} at the forward angles and 2.15×10^{-4} at the backward angles. The beam direction was determined by two methods. One was the conventional kinematical crossover method. The other was to search for the scattering angles on both sides of the beam direction at which the sign of the analyzing power of $p+^{208}$Pb elastic scattering changes sign rapidly. The uncertainty of

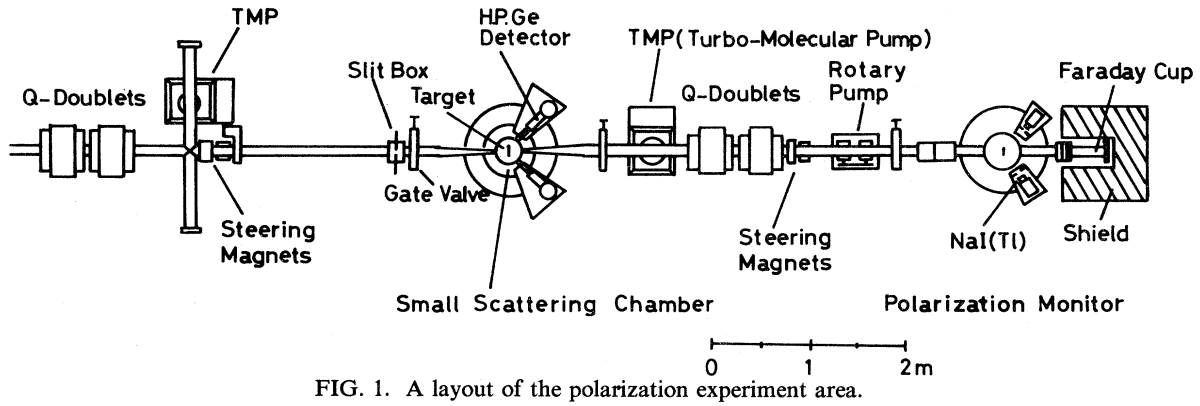

FIG. 1. A layout of the polarization experiment area.

the scattering angles was estimated to be less than ± 0.05 degrees.

The degree of beam polarization changes depending on the vacuum in the ionizer region of the PIS, the out-gassing history of the ionizer, and on other ionizer conditions. So the beam polarization was monitored continuously by a polarimeter located downstream of the scattering chamber. Scattered protons from the polarimeter target foil (a stacked 3 mg/cm^2 thick polyethylene foil) were detected by NaI(Tl) scintillators placed at $\theta_{lab}=47.5°$. The left-right asymmetry of the elastic scattering from ^{12}C was used to deduce the beam polarization. The polarimeter target foil was changed after an appropriate beam irradiation in order to reduce the effect of contaminant buildup. The beam polarization error due to the contaminant peak was estimated to be less than 0.2%. As the analyzing power of the ^{12}C polarimeter at $\theta_{lab}=47.5°$ we adopted a value of 0.975 ± 0.011, which was obtained in the double scattering experiment at $E_p=65$ MeV by Kato *et al.*[25] The direction of the proton spin was reversed after every 200 pC of integrated beam charge by reversing the solenoid magnetic field direction at the ionizer of the PIS. In the later stage of the experiment the spin direction was reversed every 1 s by alternating the atomic-beam rf transition mode between weak-field and strong-field transition. Signals from a microprocessor triggered the spin controller which controlled the rf transition mode, the scalers, and the data storage locations in the memory of the pulse height analyzer, where energy spectra were stored in different memory locations depending on the polarization direction. The average beam intensity during the measurements was about 30 nA and the beam polarization was about 60–70%. The overall energy resolution detected by the HP-Ge system was 180–250 keV FWHM, including the beam energy spread and the range straggling due to window foils of the scattering chamber, the vacuum bag, and the HP-Ge cryostat. Table I lists the forms, thicknesses, and enrichments of the target foils used. The thicknesses of the solid target foils were measured by dividing the total weight by the area, and for gas targets the gas pressure was monitored using a strain gauge sensor.

TABLE I. Targets.

Nucleus	Form	Thickness (mg/cm^2)	Enrichment
^{16}O	gas (O_2)	1–2 atm	natural (99.8%)
^{20}Ne	gas (Ne)	1–2 atm	natural (90.51%)
^{24}Mg	metal foil	3.18	99.94%
^{28}Si	metal foil	2.98	natural (92.21%)
^{40}Ar	gas (Ar)	1–2 atm	natural (99.60%)
^{46}Ca	metal foil	2.19	natural (96.97%)
^{44}Ca	metal foil	2.78	98.55%
^{48}C	$CaCO_3$ + Mylar	1.34	97.27%
^{46}Ti	metal foil	0.52	81.20%
^{48}Ca	$CaCO_3$ + Mylar	0.99	99.25%
^{50}Ti	metal foil	0.82	83.2%
^{54}Fe	metal foil	1.57	96.81%
^{56}Fe	metal foil	1.02	99.93%
^{59}Co	metal foil	2.09	99.83%
^{58}Ni	metal foil	2.04	99.83%
^{60}Ni	metal foil	2.04	99.79%
^{62}Ni	metal foil	1.71	96.48%
^{64}Ni	metal foil	3.55	96.48%
^{89}Y	metal foil	1.376	natural (100%)
^{90}Zr	metal foil	2.672	97.65%
^{98}Mo	metal foil	0.900	97.01%
^{100}Mo	metal foil	0.372	97.27%
^{144}Xm	metal foil	1.71	96.33%
^{208}Pb	metal foil	15.1	99.14%
^{209}Bi	metal foil	4.23	natural (100%)

III. DATA REDUCTION

Analyzing powers were measured by the left and right detectors located at the same scattering angle. We denote by $L_\uparrow$ the number of particles detected by the left detector in the spin up mode. $L_\downarrow$, $R_\uparrow$, and $R_\downarrow$ is defined in an analogous way. The analyzing power $A_y(\theta)$ and its statistical error $\delta A_y(\theta)$ are calculated as follows:

$$A_y(\theta)=\frac{1}{P_{\text{beam}}}\left[\frac{r-1}{r+1}\right],\quad r\equiv\left[\frac{L_\uparrow R_\downarrow}{L_\downarrow R_\uparrow}\right]^{1/2},$$

$$P_{\text{beam}}=\frac{1}{A_y(^{12}\text{C})}\left[\frac{r'-1}{r'+1}\right],\quad r'\equiv\left[\frac{L_{\uparrow\text{pol}}R_{\downarrow\text{pol}}}{L_{\downarrow\text{pol}}R_{\uparrow\text{pol}}}\right]^{1/2},$$

$$\delta A_y(\theta)=A_y(\theta)\left[\left[\frac{\delta P_{\text{beam}}}{P_{\text{beam}}}\right]^2+\left[\frac{\delta A}{A}\right]^2\right]^{1/2}$$

$$=A_y(\theta)\left[\left[\frac{\delta P_{\text{beam}}}{P_{\text{beam}}}\right]^2+\left[\frac{r^2}{r^4-1}\right]^2\left[\frac{1}{R_\uparrow}+\frac{1}{R_\downarrow}+\frac{1}{L_\uparrow}+\frac{1}{L_\downarrow}\right]\right]^{1/2},$$

$$\delta P_{\text{beam}}=P_{\text{beam}}(\theta)\left[\left[\frac{\delta A_y(^{12}\text{C})}{A_y(^{12}\text{C})}\right]^2+\left[\frac{r'^2}{r'^4-1}\right]^2\left[\frac{1}{R_{\uparrow\text{pol}}}+\frac{1}{R_{\downarrow\text{pol}}}+\frac{1}{L_{\uparrow\text{pol}}}+\frac{1}{L_{\downarrow\text{pol}}}\right]\right]^{1/2},$$

$$A_y(^{12}\text{C})=0.975,\quad \delta A_y(^{12}\text{C})=0.011,$$

where $L_{\uparrow\text{pol}}$ denotes the carbon elastic peak sum for the left polarimeter detector in the spin up mode, and $L_{\downarrow\text{pol}}$, $R_{\uparrow\text{pol}}$, and $R_{\downarrow\text{pol}}$ are similarly defined. $A_y(^{12}\text{C})$ and $\delta A_y(^{12}\text{C})$ are the carbon analyzing power and its uncertainty at the scattering angle $\theta_{\text{lab}}=47.5°$ and $E_p=65$ MeV. Differential cross section data were corrected by the detector efficiency due to nuclear reactions in the HP-Ge itself. The energy dependent detector efficiency $\epsilon(E_p)$ in the energy region from 45 to 65 MeV was obtained from Makino's data[26] according to the relation

$$\epsilon(E)=(1.0062\times10^{-3}E+1.018)^{-1}.$$

Using this formula, the difference of the elastic peak detecting efficiency between $\theta_{\text{lab}}=0°$ and $\theta_{\text{lab}}=80°$ was 0.7% for ^{16}O, and 0.3% for ^{40}Ca. Thus the correction due to Makino's data affected the relative angular distributions of the differential cross sections negligibly. Measured cross section and analyzing power data are plotted in Fig. 2. Error bars shown in the figure are only statistical ones. In the analyzing power data, uncertainties of the ^{12}C-polarimeter analyzing power are included. We notice a systematic shift of the diffraction pattern as the target mass number increases. In particular, a sharp rise near 30° in the analyzing power data shifts forward as the target mass number increases.

IV. OPTICAL POTENTIAL FITTING

Optical potential fitting to the measured data was performed using the automatic search code MAGALI of Raynal.[27] The following optical potential was used:

$$U(r)=V_{\text{Coul}}(r)-V_r f(r;r_R,a_R)-iW_v f(r;r_{wv},a_{wv})$$

$$+4a_{ws}W_s i\frac{d}{dr}f(r;r_{ws},a_{ws})$$

$$+V_{ls}\left[\frac{\hbar}{m_\pi c}\right]^2\frac{1}{r}f(r;r_{ls},a_{ls})(\vec{\sigma}\cdot\vec{\mathrm{L}}),$$

where

$$f(r;r_0,a_0)=1+\exp((r-r_0A^{1/3})/a_0)^{-1},$$

$$V_{\text{Coul}}(r)=\begin{cases}\dfrac{Ze^2}{2r_CA^{1/3}}\left[3-\dfrac{r^2}{r_C^2A^{2/3}}\right] & r\le r_C\\[2ex] \dfrac{Ze^2}{r} & r>r_C\end{cases}.$$

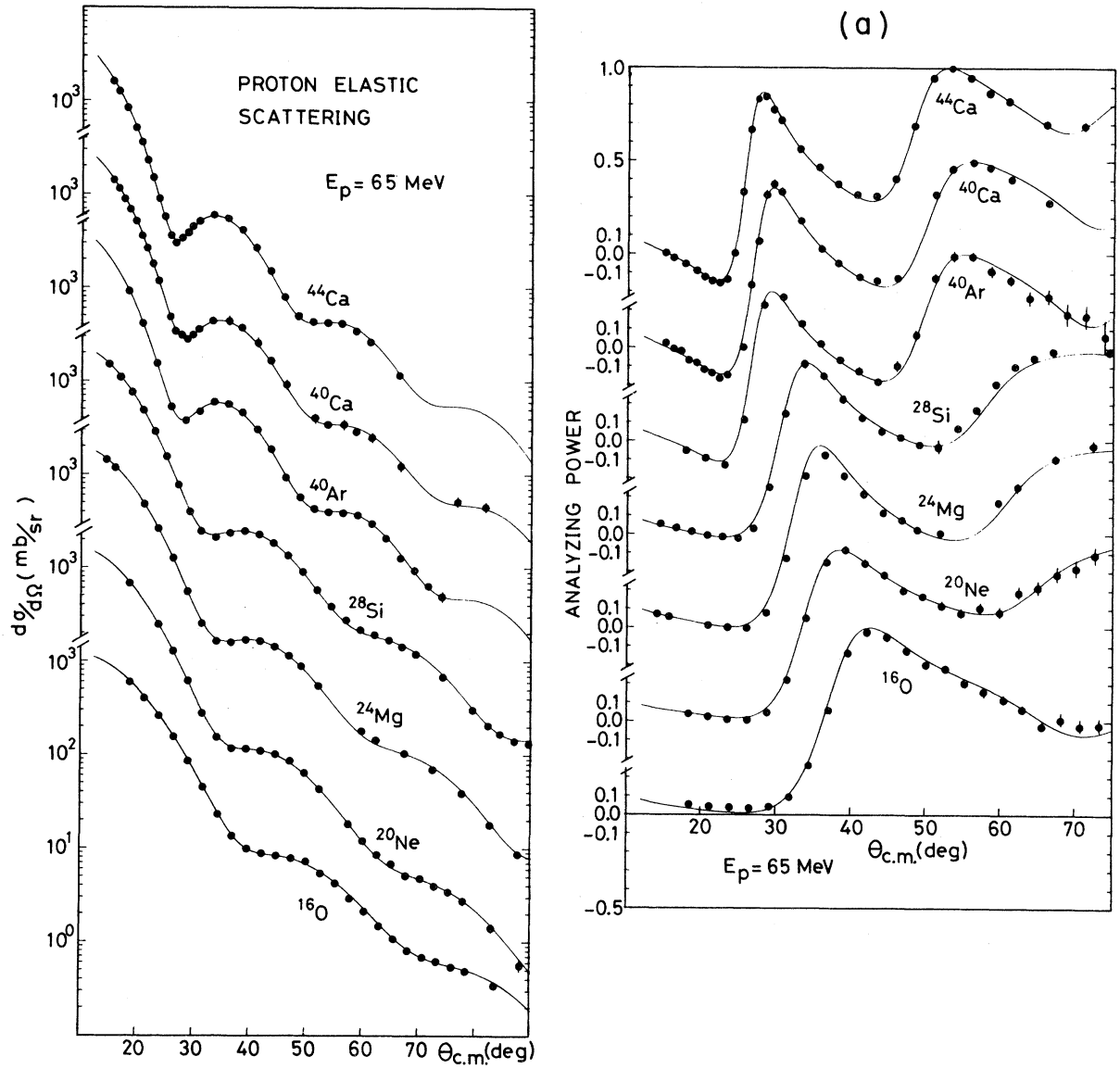

FIG. 2. (a) Measured cross sections and analyzing powers. The solid curves are optical potential calculations. The parameters used are listed in Table II. In fitting the analyzing power data, the data used were extended to $\theta_{c.m.}=90°$ for the light nuclei although only the data for $\theta_{c.m.} \leq 75°$ are shown in the figure. (b), (c), and (d) Measured cross sections and analyzing powers. The solid curves are optical potential calculations. The parameters used are listed in Table II.

A search for best-fit values of the optical potential parameters was started using the gas-target data. The probability of becoming trapped in a false local minimum during the search for a χ^2 minimum was thought to be small, since uncertainties in the cross section due to uncertainties in the target thickness measurement are small for the gas targets. For ^{40}Ar, we started with the Becchetti and Greenlees parameter values. The initial parameter values for ^{16}O, ^{20}Ne were obtained from the best-fit ^{40}Ar parameter set. For other targets, potential parameters of the neighboring target which had already been fitted were adopted as a starting set. Also, a renormalization of the calculation was introduced because of the target thickness uncertainty. In Fig. 2 measured differential cross sections and analyzing powers are shown together with the best-fit optical potential calculations. The optical potential parameters and the associated χ^2 values obtained are listed in Table II. Uncertainties in the

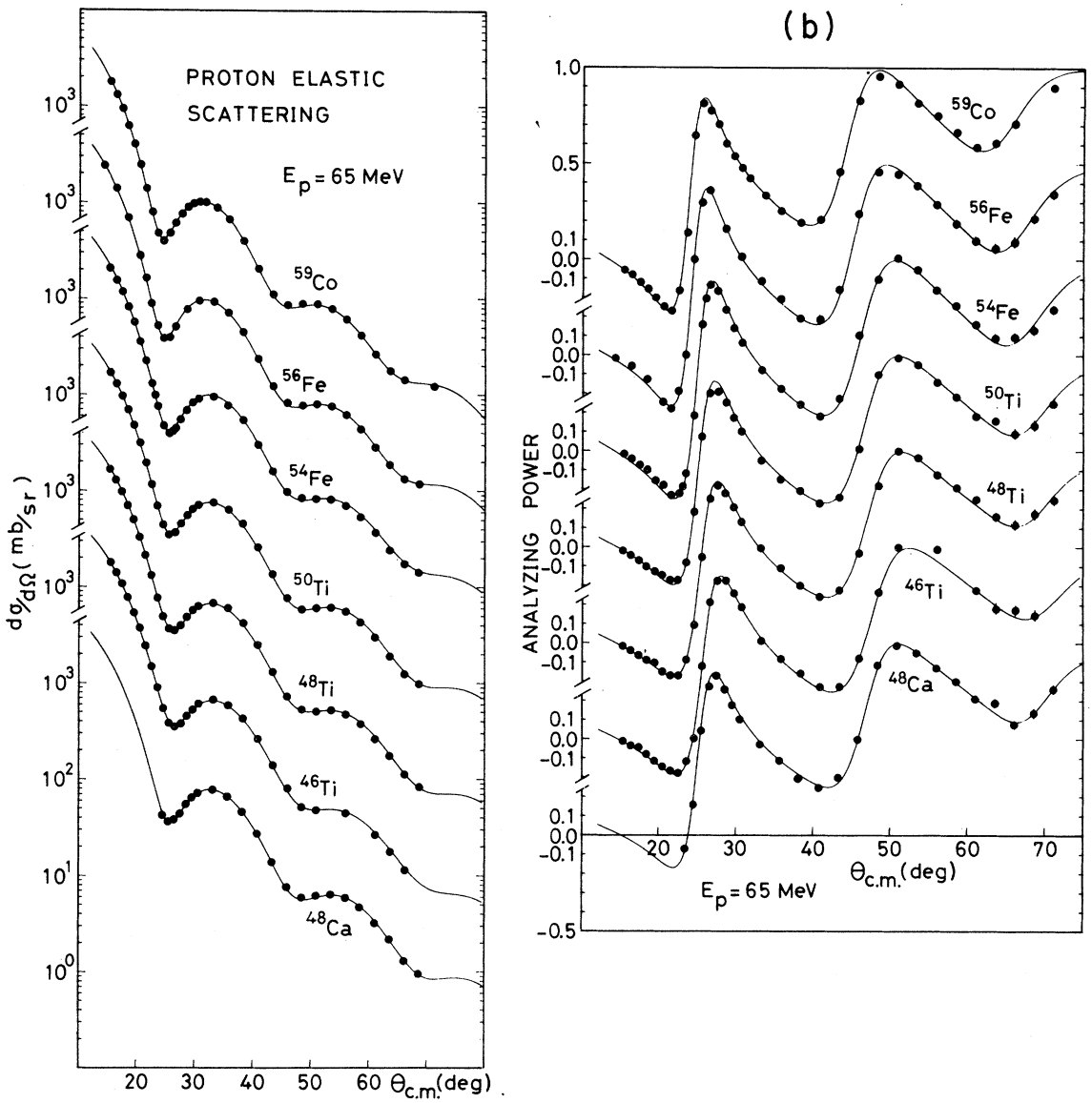

FIG. 2. (*Continued.*)

experimental data are mainly due to inhomogeneities of the target foil thickness and to scattering angle errors (less than 0.1°) rather than to counting statistics. Therefore the uncertainties used during the parameter search were

$$\delta\left[\frac{d\sigma}{d\Omega}\right]=\max\left\{0.03\times\left[\frac{d\sigma}{d\Omega}\right],\left[\frac{d\sigma}{d\Omega}\right]_{\text{statistical}}\right\}$$

and

$$\delta A(\theta)=\max\{0.03,\delta A(\theta)_{\text{statistical}}\}$$

in order to avoid trapping in an unphysical local χ^2 minimum. As for the data points in Fig. 2, the error bars for the cross sections include only the statistical errors, while the error bars for analyzing powers include the uncertainty of the ^{12}C-polarimeter analyzing power in addition.

V. SYSTEMATICS OF THE MEAN SQUARE RADIUS OF THE REAL CENTRAL PART OF THE OPTICAL POTENTIAL AND THE EFFECTIVE INTERACTION RANGE

From the real central part of the optical potential obtained in this analysis, the mean square radius of

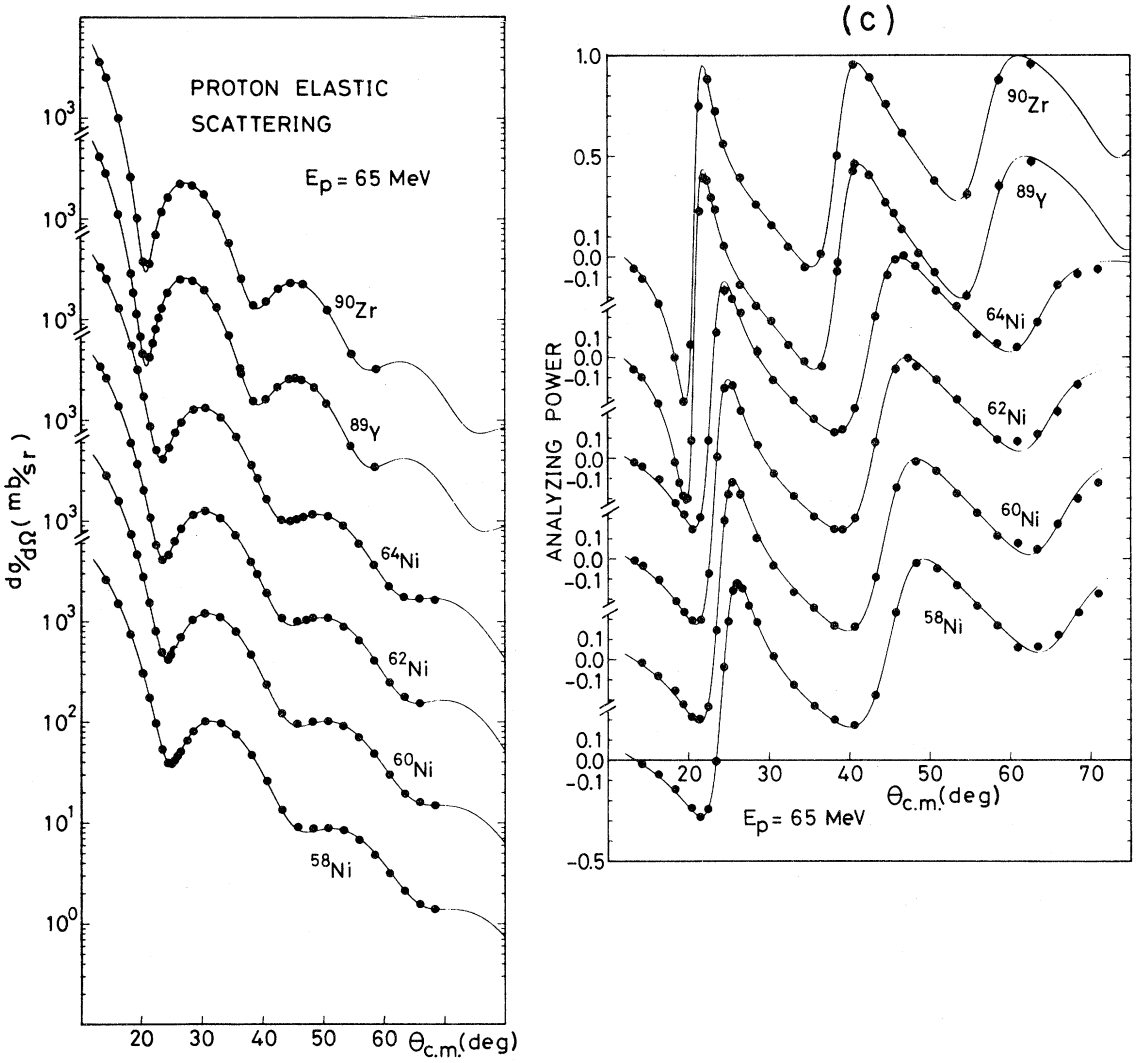

FIG. 2. (*Continued.*)

the potential, $\langle r^2\rangle_{\text{pot}}$, was calculated and is plotted as a function of $A^{2/3}$ (A denotes the target mass number) in Fig. 3. The $\langle r^2\rangle_{\text{pot}}$ data are remarkably linear in $A^{2/3}$. A linear least-squares fit to the $\langle r^2\rangle_{\text{pot}}$ data gives

$$\langle r^2\rangle_{\text{pot}}=(0.937\pm0.012)A^{2/3}+6.42\pm0.21\ \text{fm}^2\ . \tag{1}$$

The error bars in Fig. 3 indicate the uncertainties in the optical potential fitting and were calculated using the following procedure. First, all parameters except V_r and r_C were searched for to obtain the $\chi_{\min}^2(V_r)$ as a function of V_r. A $\chi_{\min}^2(V_r)$ curve for the ^{46}Ti case is shown in Fig. 4. The curve resembles a parabola. Then the error in $\langle r^2\rangle_{\text{pot}}$ was calculated from the $\langle r^2\rangle_{\text{pot}1}$ and $\langle r^2\rangle_{\text{pot}2}$ values, which were obtained with the parameter sets at $\chi_{\min}^2(V_r)=2\chi_0^2$ (best fit). Thus, the uncertainty due to the well-known VR^n=constant parameter correlation is included in the error bars.

The linear relation between $\langle r^2\rangle_{\text{pot}}$ and $A^{2/3}$ is understood in terms of a simple folding model. As was shown already by Greenlees, Pyle, and Tang,[28] the real central part of the optical potential can be written as

$$U(r_0)=\int \rho(\vec{r})V_{\text{int}}(\,|\,\vec{r}-\vec{r}_0\,|\,)d\vec{r}^{\,3}\ , \tag{2}$$

where $\rho(r)$ is the density distribution of point nucleons and $V_{\text{int}}(r)$ is an effective two-body interaction. For a nucleus with a rotationally symmetric density distribution, the mean square radius of the potential deduced from Eq. (2) is

$$\langle r^2\rangle_{\text{pot}}=\langle r^2\rangle_{\text{matt}}+\langle r^2\rangle_{\text{int}}\ , \tag{3}$$

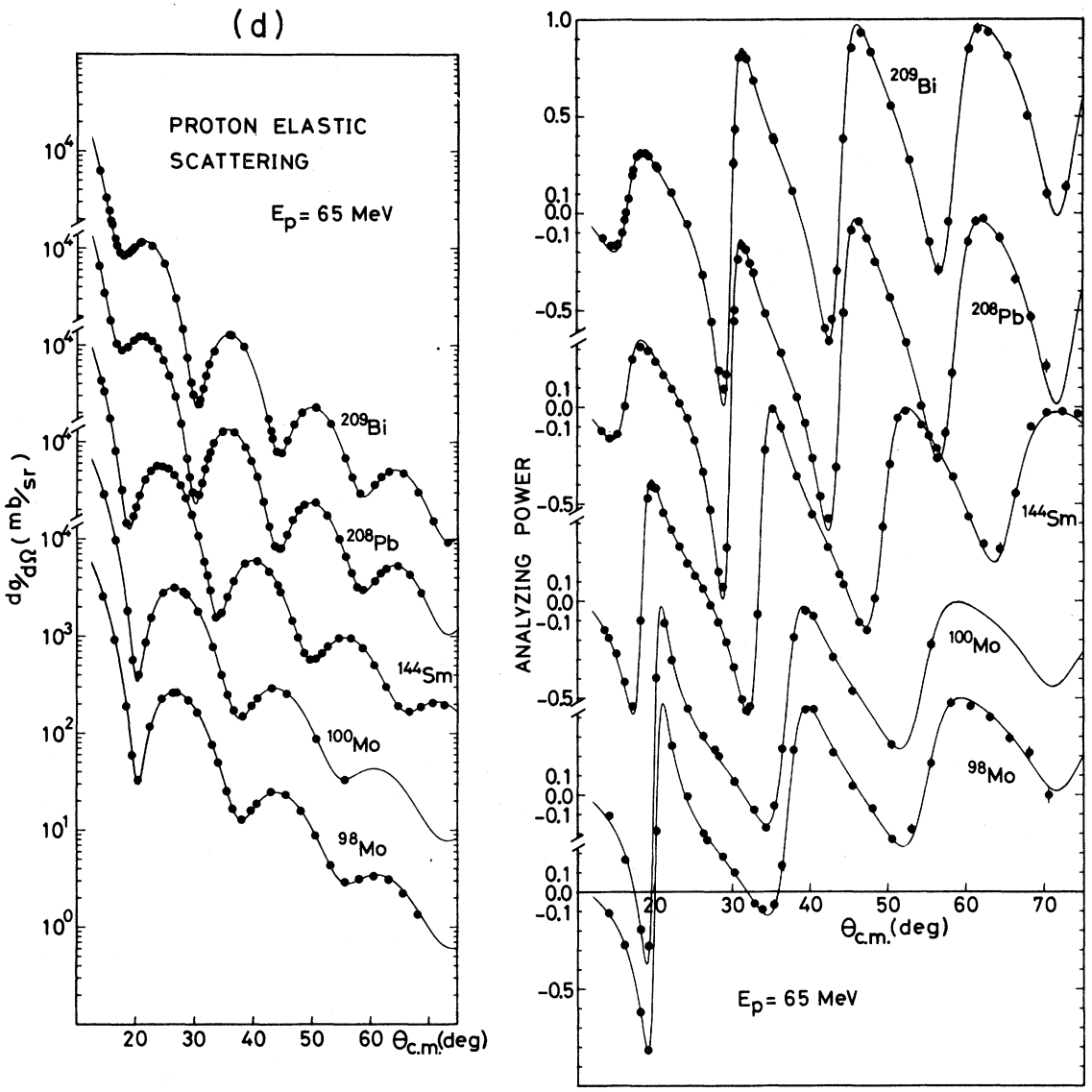

FIG. 2. (*Continued.*)

where

$$\langle r^2\rangle_{\text{pot}}=\int r^2U(\vec{r})d\vec{r}^3\Big/\int U(\vec{r})d\vec{r}^3\,,$$
$$\langle r^2\rangle_{\text{matt}}=\int r^2\rho(\vec{r})d\vec{r}^3\Big/\int \rho(\vec{r})d\vec{r}^3\,,$$

and

$$\langle r^2\rangle_{\text{int}}=\int r^2V_{\text{int}}(\vec{r})d\vec{r}^3\Big/\int V_{\text{int}}(\vec{r})d\vec{r}^3\,.$$

If we assume that $U(\vec{r})$ and $\rho(\vec{r})$ are spherically symmetric Fermi functions, $\langle r^2\rangle_{\text{matt}}$ can be calculated to a good approximation[29,30] as

$$\langle r^2\rangle_{\text{matt}}=\tfrac{3}{5}R_m{}^2+\tfrac{7}{5}\pi^2a_m{}^2\,, \tag{4}$$

where R_m and a_m are the half-density radius and diffuseness of the point-nucleon density distribution, respectively. Therefore $\langle r^2\rangle_{\text{pot}}$ is expressed as

$$\langle r^2\rangle_{\text{pot}}=\tfrac{3}{5}R_m{}^2A^{2/3}+\tfrac{7}{5}\pi^2a_m{}^2+\langle r^2\rangle_{\text{int}}\,. \tag{5}$$

In order to obtain a relation between the half-density radius and the mass number, we use the volume integral of the Fermi-type density distribution:

$$\int\rho(r)d\vec{r}^3=\frac{4\pi}{3}R_m{}^3\left[1+\frac{\pi^2a_m{}^2}{R_m{}^2}\right]\rho_0=A\,, \tag{6}$$

where

$$\rho(r)=\frac{\rho_0}{1+\exp\left[\dfrac{r-R_m}{a_m}\right]}\,.$$

TABLE II. Best fit optical potential parameters. The Coulomb radius is fixed at $r_C = 1.25$ fm.

Nucleus	V_R	r_R	a_R	W_v	r_{wv}	a_{wv}	W_s	r_{ws}	a_{ws}	V_{LS}	r_{LS}	a_{LS}	χ^2/F	Renorm. factor
^{16}O	27.172	1.297	0.6556	12.847	0.2762	1.198	3.290	1.350	0.375	5.793	1.057	0.5807	1.50	1.04
^{20}Ne	31.162	1.212	0.7439	7.709	0.9552	0.9484	2.658	1.320	0.5367	5.402	1.015	0.6860	1.25	1.05
^{24}Mg	27.242	1.251	0.6864	10.525	0.8908	1.041	1.809	1.395	0.3850	5.269	1.022	0.6364	2.29	1.23
^{28}Si	33.912	1.176	0.7248	9.917	0.8388	0.3660	5.348	1.241	0.5656	5.970	1.007	0.6181	1.68	1.05
^{40}Ar	34.249	1.208	0.7266	9.063	1.137	0.7498	2.897	1.357	0.4928	5.606	1.061	0.6722	1.64	1.07
^{40}Ca	33.285	1.232	0.7080	8.131	1.164	0.7993	2.737	1.344	0.4413	5.796	1.088	0.6317	0.806	0.807
^{44}Ca	31.474	1.246	0.7007	9.703	1.120	0.9099	2.553	1.329	0.4476	5.499	1.094	0.6554	1.16	0.956
^{48}Ca	32.907	1.230	0.6808	10.228	1.187	0.7824	2.515	1.344	0.3975	5.680	1.091	0.6475	0.792	1.03
^{46}Ti	31.691	1.241	0.7082	8.034	1.182	0.8090	2.376	1.347	0.4949	5.285	1.094	0.6554	0.772	1.03
^{48}Ti	31.425	1.242	0.7041	8.244	1.191	0.8346	2.189	1.349	0.4199	5.209	1.094	0.6554	0.608	0.955
^{50}Ti	32.610	1.226	0.6898	9.521	1.162	0.8216	2.506	1.346	0.3941	5.248	1.083	0.6276	0.550	0.982
^{54}Fe	33.195	1.212	0.6907	10.410	1.047	0.7670	2.922	1.330	0.4803	5.608	1.071	0.6155	0.550	1.11
^{56}Fe	34.870	1.197	0.7138	11.354	1.004	0.8162	3.333	1.316	0.5307	5.581	1.051	0.6285	0.678	1.01
^{59}Co	33.634	1.212	0.7177	9.606	1.133	0.8240	2.231	1.346	0.4654	5.559	1.071	0.6554	0.610	0.966
^{58}Ni	35.466	1.173	0.7248	12.499	0.9729	0.6262	3.618	1.319	0.5639	5.907	1.027	0.6554	0.511	1.08
^{60}Ni	34.812	1.195	0.7171	11.662	1.001	0.8083	3.282	1.317	0.5345	5.781	1.049	0.6554	0.439	1.11
^{62}Ni	33.831	1.218	0.7175	11.356	1.052	0.8815	3.195	1.320	0.4562	5.757	1.074	0.6554	0.638	1.04
^{64}Ni	33.858	1.209	0.7234	11.518	1.019	0.7744	3.864	1.310	0.5422	5.822	1.063	0.6554	0.696	1.02
^{89}Y	35.463	1.232	0.7084	8.545	1.274	0.7226	2.806	1.301	0.3847	5.506	1.147	0.6300	0.918	1.06
^{90}Zr	34.861	1.233	0.7129	9.230	1.223	0.7070	2.621	1.352	0.4180	5.395	1.138	0.6527	0.498	0.936
^{98}Mo	34.460	1.240	0.7407	8.585	1.016	0.8210	5.163	1.261	0.6046	5.035	1.147	0.6603	0.729	0.951
^{100}Mo	34.933	1.244	0.7311	7.058	1.072	0.7878	5.901	1.248	0.6005	5.267	1.156	0.6339	0.283	1.08
^{144}Sm	36.162	1.230	0.7288	10.439	1.016	0.8210	5.676	1.248	0.6005	5.397	1.151	0.6224	0.584	1.10
^{208}Pb	39.105	1.223	0.7461	9.816	1.142	0.7775	5.758	1.253	0.5872	5.838	1.175	0.6103	0.652	1.13
^{209}Bi	37.399	1.229	0.7347	12.160	1.016	0.8210	6.236	1.252	0.5998	5.447	1.155	0.6330	0.696	1.09

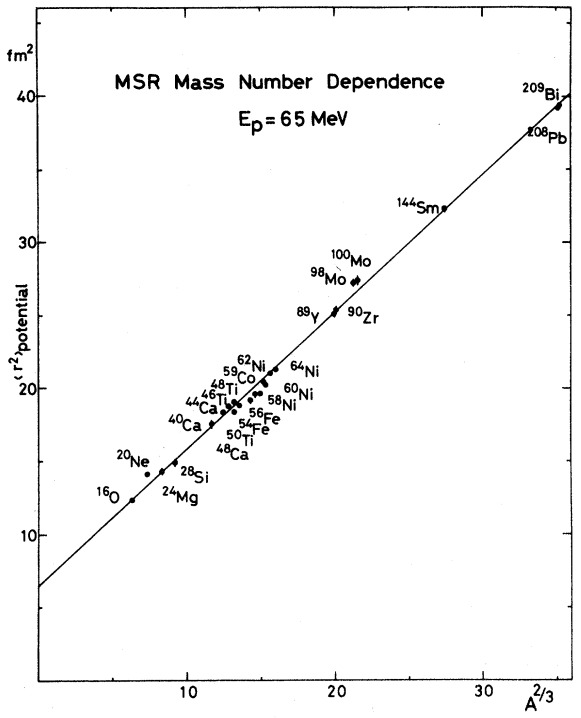

FIG. 3. Mean square radii of the real central part of the optical potentials are shown as a function of the target mass number A. The definition of the error bars in the figure is explained in the text. The numerical data with error bars are listed in Table III. The solid line is obtained by least-square linear fitting to the data.

Since a_m and ρ_0 are reasonably constant with A, the half-density radius R_m is calculated as a function of A, as

$$R_m = r_m A^{1/3}\left\{1-\frac{1}{3}\left[\frac{\pi^2 a_m{}^2}{r_m{}^2 A^{2/3}}\right] + \frac{1}{81}\left[\frac{\pi^2 a_m{}^2}{r_m{}^2 A^{2/3}}\right]^3 + \cdots\right\}, \quad (7)$$

where

$$r_m = \left[\frac{3}{4\pi\rho_0}\right]^{1/3}.$$

Inserting (7) into (5), we obtain for $\langle r^2\rangle_{\rm pot}$

$$\langle r^2\rangle_{\rm pot} = \langle r^2\rangle_{\rm int} + \tfrac{3}{5} r_m{}^2 A^{2/3} + \pi^2 a_m{}^2 + \tfrac{1}{15}\pi^2 a_m{}^2\left[\frac{\pi^2 a_m{}^2}{r_m{}^2 A^{2/3}}\right] + \cdots . \quad (8)$$

The last term can be neglected since the ratio of the 4th term to the 3rd term is less than 0.02 for the nuclei considered ($A \geq 16$). We finally obtain an approximate relation

$$\langle r^2\rangle_{\rm pot} = \tfrac{3}{5} r_m{}^2 A^{2/3} + \pi^2 a_m{}^2 + \langle r^2\rangle_{\rm int} . \quad (9)$$

If we treat $\langle r^2\rangle_{\rm int}$ as a constant as usual, $\langle r^2\rangle_{\rm pot}$ is linear in $A^{2/3}$, with the coefficient $\frac{3}{5} r_m{}^2$. In order

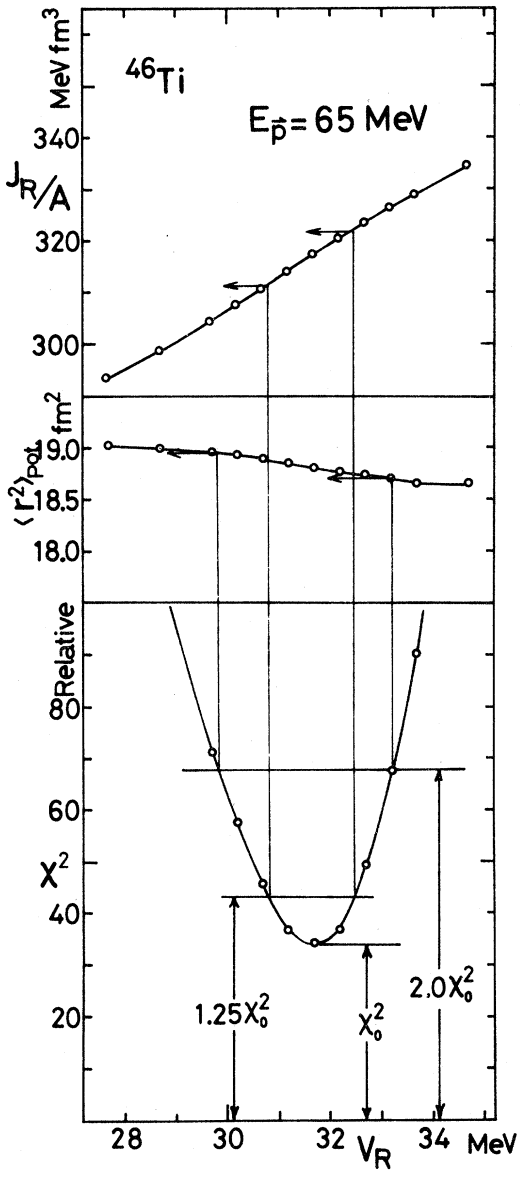

FIG. 4. An example of the procedure for deducing the error bars is shown. The volume integral per nucleon of the real central part of the optical potential, the mean square radius of the potential, and the total χ^2 value are plotted as a function of the potential depth V_R for ^{46}Ti. For $\langle r^2\rangle_{\rm pot}$, error bars are obtained from the 2 $\chi_0{}^2$ point and for J_R/A from the 1.25 $\chi_0{}^2$ point.

to obtain the $\langle r^2\rangle_{\rm int}$ value, we need to know the a_m value, which is inferred from the charge distribution data. By comparing the two linear relations (1) and (9), we obtain the value of

$$r_m=(1.25\pm0.01)\ \text{fm}\ .$$

If we assume that the point proton density distribution is also of the Fermi-type (as we did for the nuclear matter distribution), then $\langle r^2\rangle_{\rm charge}$ can be written in terms of the half-density radius R_p and the diffuseness a_p of the point proton distribution, and the mean square radius of the charge distribution of the proton itself, $\langle r^2\rangle_{\rm proton}$, as

$$\langle r^2\rangle_{\rm charge}=\tfrac{3}{5}R_P{}^2+\tfrac{7}{5}\pi^2a_p{}^2+\langle r^2\rangle_{\rm proton}\ . \quad (10)$$

For a relation between R_p and the mass number A, we use the same relation as (7):

$$R_p=r_pA^{1/3}\left\{1-\frac{1}{3}\left[\frac{\pi^2a_m{}^2}{r_m{}^2A^{2/3}}\right]+\frac{1}{81}\left[\frac{\pi^2a_m{}^2}{r_m{}^2A^{2/3}}\right]^3+\cdots\right\}. \quad (11)$$

We finally obtain a linear relation for $\langle r^2\rangle_{\rm charge}$ with $A^{2/3}$:

$$\langle r^2\rangle_{\rm charge}=\tfrac{3}{5}r_p{}^2A^{2/3}+\pi^2a_p{}^2+\langle r^2\rangle_{\rm proton}\ . \quad (12)$$

The mean square radius of the charge distribution, $\langle r^2\rangle_{\rm charge}$, from electron scattering[31] is plotted in Fig. 5 as a function of $A^{2/3}$. By least-squares linear fitting, we obtained

$$\langle r^2\rangle_{\rm charge}=(0.799\pm0.006)A^{2/3}+(2.50\pm0.12)\ \text{fm}^2\ .$$

By introducing the $\langle r^2\rangle_{\rm proton}=0.64$ fm^2 and comparing values from electron scattering with Eq. (12), we obtain

$$r_p=(1.154\pm0.004)\ \text{fm}$$

and

$$a_p=(0.434\pm0.012)\ \text{fm}\ .$$

These values are slightly modified by taking into account the neutron charge distribution.[31] Thus

$$r_p=(1.158\pm0.004)\ \text{fm}$$

and

$$a_p=(0.397\pm0.011)\ \text{fm}$$

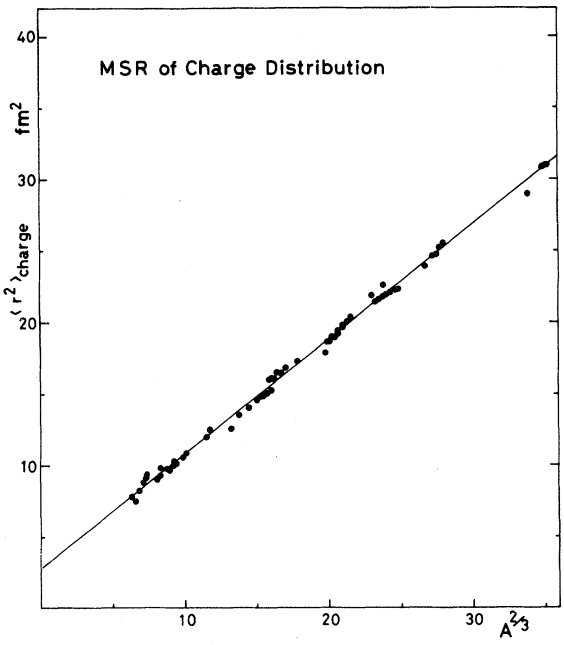

FIG. 5. Mean square radii of charge distributions obtained from electron scattering are plotted as a function of the mass number A.

are obtained. If the diffuseness of the point nucleon distribution is assumed to be equal to the diffusenss of the point proton distribution, we get the value of

$$\langle r^2\rangle_{\rm int}=(4.24\pm0.24)\ \text{fm}^2\ .$$

We notice that the value of r_m extracted from the present experiment is larger than that of r_p obtained from the electron scattering data. In order to show that such a difference is common to proton scattering, linear fits were made to the mean square potential radii from Perey's collection[32] of optical potential results at 27–32 MeV incident proton energies. These are shown in Fig. 6. The values obtained are

$$r_m=(1.21\pm0.03)\ \text{fm}$$

and

$$\langle r^2\rangle_{\rm int}=(4.06\pm0.84)\ \text{fm}^2$$

at 30 MeV. Although the 30 MeV data consist of optical potential parameters by many authors and hence could contain many inconsistencies among the parameters obtained due to different fitting principles, the r_m and $\langle r^2\rangle_{\rm int}$ values from the 30 MeV data are consistent with our values, and r_m is larger than the r_p value of 1.158 fm. From the analysis of the 800 MeV-1 GeV data,[33–42] it is con-

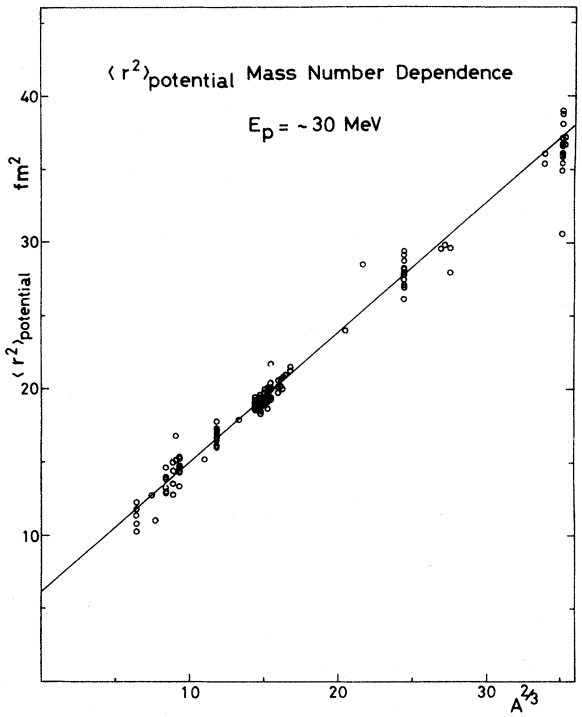

FIG. 6. Mean square radii of the real central part of the optical potentials of the collection of Perey and Perey at $E_p=27-32$ MeV are plotted as a function of $A^{2/3}$.

cluded that r_m is approximately equal to r_p.

One answer to this contradiction is to introduce a target mass number dependence into the effective interaction range $\langle r^2\rangle_{\rm int}$. As demonstrated in Fig. 3, the linear relation between $\langle r^2\rangle_{\rm pot}$ and $A^{2/3}$ is confirmed and acceptable. Therefore the mass number dependence to be introduced into $\langle r^2\rangle_{\rm int}$ must also be linear in $A^{2/3}$. A recent argument[33] based on experimental data,[34–36] and the experimental results[37–42] from the Los Alamos Meson Physics Facility (LAMPF), show that with a small correction from the charge distribution in the neutron itself, the difference between the root mean square radius of the point nucleon distribution and that of the point proton distribution is less than 0.1 fm, which is smaller than the error in our $\langle r^2\rangle_{\rm int}$ value. Thus the average density distribution of point nucleons may be thought to be equal to that of point protons. Then the effective two-body interaction range obtained is

$$\langle r^2\rangle_{\rm int}=4.24\pm0.24 + (0.132\pm0.013)A^{2/3}\ \text{fm}^2 .$$

According to the recent theoretical work of Brieva[5–8] on the nucleon-nucleus optical potential using a realistic nucleon-nucleon interaction, the exchange term is repulsive in the nuclear center, whereas at the surface it is attractive. An exchange term of this type introduces a mass number dependence of the effective interaction range if $\langle r^2\rangle_{\rm pot}$ is defined as

$$\langle r^2\rangle_{\rm int}=\langle r^2\rangle_{\rm pot}-\langle r^2\rangle_{\rm charge}+\langle r^2\rangle_{\rm proton} .$$

Another source of the mass number dependence may come from a small difference between the point proton and the point neutron distributions, because the proton-neutron interaction is stronger than the proton-proton interaction, and this fact may enhance the effect from the density distribution difference. Thus the mass number dependence of $\langle r^2\rangle_{\rm int}$ is an empirical relation and reflects various many-body effects. The true origin of this mass number dependence may be explained by an elaborate microscopic calculation. The possibility of a target dependence of the effective interaction range has been suggested already by Sinha.[30] Our $\langle r^2\rangle_{\rm int}$ value is larger than the GPT's value[28] of (2.25 ± 0.6) fm^2. GPT's $\langle r^2\rangle_{\rm int}$ value was obtained in the search for the χ^2 minimum mainly of the cross section data because of the partial lack of polarization data at that time. By equally weighting the polarization and cross section data we were able to reduce the VR^n-type ambiguity and have found a larger value for the mass number dependent $\langle r^2\rangle_{\rm int}$. Bertsch *et al.*[43] also obtained a large $\langle r^2\rangle$ value ($\sim$6 fm^2) for inelastic scattering by fitting the interaction to the matrix element of the scattering operator, the t matrix or G matrix. Since their interaction is effective at the nuclear surface and is not density dependent, their $\langle r^2\rangle_{\rm int}$ does not have any mass number dependence. Our $\langle r^2\rangle_{\rm int}$ values for medium-weight nuclei are as large as the one obtained in the Bertsch calculation.[43]

VI. COMPARISON BETWEEN EXPERIMENTAL $\langle r^2\rangle_{\rm pot}$ VALUES AND MICROSCOPIC CALCULATIONS

In the preceding section it was pointed out that there is a difference between $\langle r^2\rangle_{\rm matt}$ and $\langle r^2\rangle_{\rm pot}$ in the target mass number dependence. This difference was reduced to the mass number dependence of the effective two-body interaction. In Fig. 7 the calculated values based on the recent microscopic theories are shown with the experimental $\langle r^2\rangle_{\rm pot}$ values. The line labeled JLM is the calculation using the JLM model. A detailed explanation of the

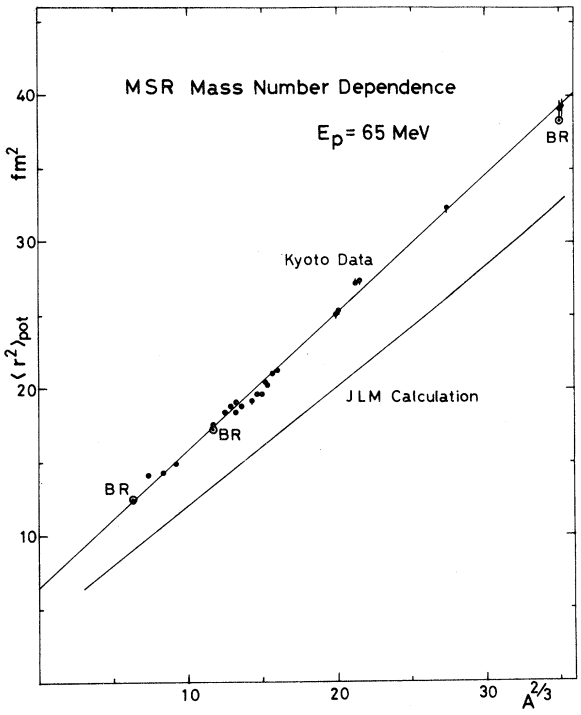

FIG. 7. Mean square radii deduced from the best-fit optical potential are compared with the recent microscopic optical potential calculations. The ⊙ symbols denote Brieva-Rook values interpolated to $E_p = 65$ MeV. The solid line marked JLM is obtained from the optical potential with the microscopically-derived parameters of Jeukenne, Lejeune, and Mahaux.

JLM calculation will be given in Sec. VIII. Brieva and Rook calculated the $\langle r^2 \rangle_{pot}$ values of ^{16}O, ^{40}Ca, and ^{206}Pb for several incident energies and their $\langle r^2 \rangle_{pot}$ values varied smoothly with energy. The points labeled BR show the interpolation to 65 MeV proton energy of the BR calculations. The BR calculation reproduces remarkably our experimental values shown as the line labeled Kyoto data, although the BR value for ^{208}Pb is a little smaller than the observed value. Calculations in the JLM model differ greatly from the experimental values (by 2–5 fm^2) and cannot reproduce the slope of the mass number dependence. Lejeune and Hodgson[44] pointed out that the JLM calculation does not explain the $\langle r^2 \rangle_{pot}$ values and angular distributions and must be modified by introducing a phenomenological range parameter. Such a phenomenological parameter, however, will mask the validity of the theory to study the dynamics of the reaction. The main origin of the discrepancy may be in the LDA approximation used to transform the optical potential in nuclear matter to the optical potential in a finite nucleus. These two types of microscopic calculations suggest that the density dependence of the effective two-body interaction at the nuclear surface plays an essential role in explaining the A dependence of the $\langle r^2 \rangle_{int}$ value. It was already pointed out in nuclear matter theory that there is a density dependence[44] in the nuclear matter effective interaction. As the density decreases, the effective two-body interaction increases due to the Pauli principle, and the depth of the optical potential well increases. But the A dependence of $\langle r^2 \rangle_{int}$ is not explained by the density-dependent JLM interaction using the LDA alone, because the slope of the JLM calculation on the target mass number A is different from the experimentally observed one (see Fig. 7). On the other hand, when obtaining the t matrix in the r representation in the BR calculation, the momentum sum up to the Fermi momentum gives another contribution to the density dependence[45] of the interaction, in addition to the dependence coming explicitly from the Pauli principle. From our present knowledge of the BR calculation, however, we cannot discern the primary origin of the A dependence of the $\langle r^2 \rangle_{int}$.

VII. ROOT MEAN SQUARE RADIUS OF THE POINT NUCLEON DISTRIBUTION OF THE TARGET NUCLEUS

Applying the results obtained in the preceding section, we can extract the root mean square radius of the point nucleon distribution of the target nucleon, as follows

$$\langle r^2 \rangle_{matt}^{1/2} = (\langle r^2 \rangle_{potential} - \langle r^2 \rangle_{int})^{1/2} .$$

where

$$\langle r^2 \rangle_{int} = 4.24 \pm 0.24 + (0.13 \pm 0.013) A^3 \text{ fm}^2 .$$

The calculated $\langle r^2 \rangle_{matt}^{1/2}$ values from our elastic scattering data are listed in Table III, together with the 800 MeV polarized proton elastic scattering results from LAMPF. The LAMPF $\langle r^2 \rangle_{matt}^{1/2}$ values were calculated from the proton MSR values $\langle r^2 \rangle_p$ and the neutron MSR values $\langle r^2 \rangle_n$ of their data,[38–42] using the relation

$$\langle r^2 \rangle_{matt}^{1/2} = \left[\frac{N}{A} \langle r^2 \rangle_n + \frac{Z}{A} \langle r^2 \rangle_p \right]^{1/2} .$$

Although the LAMPF $\langle r^2 \rangle_n$ and $\langle r^2 \rangle_p$ values are model dependent, they are thought to be relatively free from the dynamical effects on the nucleon-nucleon interaction in the nucleus. We no-

TABLE III. Values deduced from the optical potential parameters. The volume integral per nucleon and mean square radius of the real central part of the optical potential are listed, together with their respective errors. The effective interaction range and the nuclear matter radius are listed and compared with LAMPF values. The LAMPF values are calculated using

$$\langle r^2\rangle_{\text{matt}}^{1/2}=\left[\frac{N}{A}\langle r^2\rangle_n+\frac{Z}{A}\langle r^2\rangle_p\right]^{1/2}.$$

Nuclei	J_R/A (MeV fm^3)	$\langle r^2\rangle_{\text{pot}}$ (fm^2)	$\langle r^2\rangle_{\text{int}}$ (fm^2)	$\langle r^2\rangle^{1/2}$ (fm) Kyoto	LAMPF
^{16}O	$346.8^{+14.2}_{-9.4}$	$12.35^{+0.06}_{-0.26}$	5.08	2.70	
^{20}Ne	$349.5^{+9.64}_{-11.3}$	$14.14^{+0.02}_{-0.06}$	5.21	2.99	
^{24}Mg	$303.0^{+15.3}_{-14.5}$	$14.32^{+0.07}_{-0.23}$	5.34	3.00	
^{28}Si	$325.3^{+7.8}_{-14.0}$	$14.92^{+0.06}_{-0.07}$	5.46	3.08	
^{40}Ar	$330.4^{+7.4}_{-11.5}$	$17.54^{+0.05}_{-0.28}$	5.78	3.43	
^{40}Ca	$333.6^{+5.2}_{-8.6}$	$17.58^{+0.01}_{-0.18}$	5.78	3.43	3.39
^{44}Ca	$318.8^{+5.7}_{-8.5}$	$18.39^{+0.03}_{-0.18}$	5.89	3.54	3.48
^{48}Ca	$315.0^{+6.9}_{-7.5}$	$18.39^{+0.07}_{-0.09}$	5.98	3.52	3.47
^{46}Ti	$317.24^{+4.6}_{-5.9}$	$18.79^{+0.16}_{-0.10}$	3.93	3.59	
^{48}Ti	$313.1^{+4.9}_{-4.0}$	$19.08^{+0.06}_{-0.10}$	5.98	3.62	
^{50}Ti	$309.7^{+5.3}_{-3.5}$	$18.82^{+0.08}_{-0.03}$	6.03	3.58	
^{54}Fe	$303.1^{+5.9}_{-5.1}$	$19.18^{+0.14}_{-0.24}$	6.13	3.61	3.57
^{56}Fe	$307.1^{+2.8}_{-3.2}$	$19.69^{+0.07}_{-0.16}$	6.17	3.68	
^{59}Co	$307.8^{+4.6}_{-4.0}$	$20.47^{+0.09}_{-0.09}$	6.24	3.77	
^{58}Ni	$300.2^{+2.6}_{-2.0}$	$19.63^{+0.06}_{-0.20}$	6.22	3.66	3.67 or 3.70
^{60}Ni	$306.8^{+2.1}_{-3.4}$	$20.25^{+0.07}_{-0.12}$	6.26	3.74	
^{62}Ni	$309.4^{+5.1}_{-5.0}$	$21.07^{+0.21}_{-0.19}$	6.31	3.84	
^{64}Ni	$315.1^{+3.3}_{-3.2}$	$21.27^{+0.21}_{-0.19}$	6.35	3.86	3.86
^{89}Y	$323.4^{+2.7}_{-2.4}$	$25.09^{+0.1}_{-0.35}$	6.87	4.27	
^{90}Zr	$318.9^{+1.3}_{-4.4}$	$25.35^{+0.19}_{-0.41}$	6.89	4.30	4.25
^{98}Mo	$321.0^{+2.7}_{-5.8}$	$27.20^{+0.30}_{-0.13}$	7.05	4.49	
^{100}Mo	$326.0^{+3.4}_{-1.0}$	$27.38^{+0.61}_{-0.31}$	7.08	4.51	
^{144}Sm	$317.4^{+3.4}_{-2.2}$	$32.18^{+0.23}_{-0.39}$	7.87	4.93	
^{208}Pb	$330.7^{+2.3}_{-7.0}$	$39.18^{+0.64}_{-0.064}$	8.87	5.51	5.55
^{209}Bi	$319.7^{+3.3}_{-3.6}$	$39.36^{+0.46}_{-0.71}$	8.89	5.52	

tice in Table III that our values agree remarkably well with the LAMPF results. This indicates the validity of our procedure for extracting the $\langle r^2\rangle_{\text{int}}$ value and the mass number dependence of the effective interaction range. We have thus obtained a new method for extracting $\langle r^2\rangle_{\text{matt}}^{1/2}$ value from polarized proton elastic scattering.

VIII. THE VOLUME INTEGRAL OF THE REAL CENTRAL PART OF THE OPTICAL POTENTIAL

In the folding model the volume integral J_R of the real central part of the optical potential is calculated as

$$J_R=\int V(\vec{r}_0)d\vec{r}_0{}^3$$
$$=\int d\vec{r}_0{}^3\int d\vec{r}^{\,3}(r)V_{\text{int}}(|\vec{r}-\vec{r}_0|)$$
$$=A\int V_{\text{int}}(\vec{a})d\vec{a}^{\,3}.$$

The volume integral value J_R is proportional to the target mass number if the effective two-body interaction potential between the projectile and the target nucleon is independent of density and energy. A linear fit to the J_R values confirms the approximate validity of the above assumption at 65 MeV, and the volume integral is expressed as

$$J_R(318\pm3)A \text{ MeV fm}^3.$$

In order to show how the recent microscopic calculations explain the empirical volume integral values, J_R/A values are plotted as a function of incident proton energy in Fig. 8. The double-circle point at 65 MeV is the average value of the Kyoto data. The open circles show the recent measurement for ^{40}Ca by the Milan group.[13,14] We notice that the Kyoto data lie on a smooth extrapolation of lower-energy Milan data. The solid and dashed curves labeled JLM indicate the volume integral of the microscopic optical potential calculated in the JLM model. According to the parameter table of the JLM calculation,[4] the optical potential in infinite nuclear matter is obtained as a function of the matter density and the incident projectile energy. As for the point nucleon density distribution for the JLM calculation, we used Negele's density distribution[11] obtained from fitting electron scattering data, as in the JLM work. The solid curve shows the calculation for ^{208}Pb and the dashed curve shows the ^{40}Ca case. The results of the Brieva-Rook calculation are indicated by the points marked with a cross in the figure for ^{40}Ca and ^{208}Pb nuclei; the curves connecting these points are only meant to guide the eye. As is evident from the figure, the J_R/A value and its bombarding energy dependence are reproduced remarkably well by the JLM calculation. The local density approximation used in the JLM model seems to be effective for the J_R calculation.

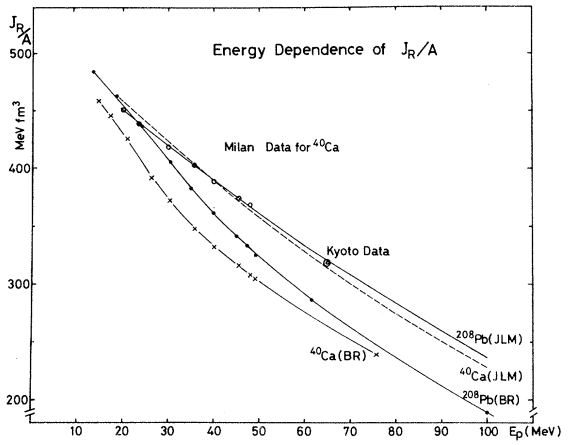

FIG. 8. Volume integral values per nucleon of the optical potential are plotted as a function of incident proton energy. Open circles are Milan data for ^{40}Ca, and the double circle is a mean value over 25 targets at $E_p=65$ MeV. The solid dots and the crosses are values calculated microscopically by Brieva and Rook, connected by curves meant to guide the eye. The solid and broken curves labeled JLM are calculated values using the procedure of Jeukenne, Lejeune, and Mahaux.

The energy dependence and the density dependence of the nuclear matter t matrix are directly reflected in the JLM nuclear optical potential. On the other hand, Brieva and Rook transformed the nuclear matter t matrix in momentum representation to the t matrix in the r representation using a suitable approximation. They then calculated the optical potential for finite nuclei by applying the folding approximation. The calculations of BR explain empirical results at 30 MeV, but deviate from the observed values at higher energies. The origin of the discrepancy between the BR calculation and the experimental data seems to be due to the approximation in their transformation to the r representation.

In Fig. 9 our J_R/A values listed in Table III are plotted as a function of the target mass number. Error bars in the figure were defined similar to the error bars of $\langle r^2\rangle_{\rm pot}$ values in Sec. V but in this case were deduced from the potential parameters at $\chi_{\rm min}^2(V_r)=1.25\chi_0^2$ (best fit), so the error bars have no statistical meaning. Although the observed J_R/A values scatter considerably, we notice the following global behavior around the average value of $J_R/A=318$ MeV. As the mass number A increases, J_R/A decreases rapidly to the minimum in the Fe-Ni region and then increases gradually towards the Pb-Bi region. This global trend is remarkably reproduced by the JLM model calculation shown by the dashed curve in Fig. 9. According to the JLM model, the effective interaction is density dependent. In the lower-density region, the effective interaction is stronger[3,4] due to the smaller Pauli blocking effect. The surface-to-volume ratio is large in light nuclei. As the target mass number in-

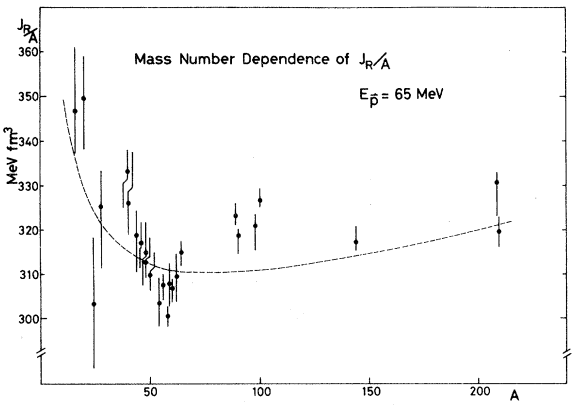

FIG. 9. Volume integral values per nucleon of the real central part of the optical potentials are plotted as a function of the target mass number A. The definition of the error bars is given in the text. The dashed curve is the JLM model calculation for $E_p=65$ MeV.

creases, the surface-to-volume ratio decreases as $A^{-1/3}$ and the J_R/A value decreases rapidly. The second gradual increase is explained in the JLM model by the isospin dependent interaction and by the velocity dependence of the effective interaction (as the mass number increases, the velocity of the projectile inside the nucleus decreases due to the repulsive Coulomb potential.) This global trend in Fig. 9 is similar to the binding energy per nucleon curve if we note that the Coulomb potential is included in the binding energy calculation and the velocity dependent effect is included in the J_R/A calculation. The rapid change in J_R/A values for lighter nuclei evident in Fig. 9 is possibly evidence of the density dependence of the effective interaction.

IX. CONCLUSIONS

We have systematically measured polarized proton elastic scattering from 25 targets at 65 MeV. An optical potential analysis gave good fits to both cross section and analyzing power data. By plotting the mean square radius of the real central part of the optical potential versus $A^{2/3}$, we have obtained the global systematics of the MSR of the potential as

$$\langle r^2\rangle_{\text{pot}}=(0.937\pm0.012)A^{2/3}+(6.42\pm0.21)\ \text{fm}^2 .$$

Using the simple folding model and comparing with charge distributions obtained from electron scattering, we found that the effective interaction range has a mass number dependence of the form

$$\langle r^2\rangle_{\text{int}}=(4.24\pm0.24)+(0.132\pm0.013)A^{2/3}\ \text{fm}^2 .$$

Assuming this mass number dependence of the effective interaction range, we have obtained root mean square radii of the point nucleon distributions, which are in accord with the high-energy LAMPF data and reflect the shell effect and the individual characteristics of the target nuclei.

For nuclei of $A<58$, the J_R/A value decreases as the mass number of the target increases. This rapid decrease was interpreted as evidence of the density dependence of the effective interaction. The JLM model explains both the energy and A dependence of J_R but cannot explain the value of $\langle r^2\rangle_{\text{pot}}$ and its A dependence.

On the other hand, the BR calculation reproduces our $\langle r^2\rangle_{\text{pot}}$ value but could not predict the J_R values, especially the energy dependence of J_R. At present, each of the two global theories could explain the experimental results only partially, but is found to be an effective guide in clarifying nuclear many-body dynamics.

ACKNOWLEDGMENTS

The authors wish to express their thanks to Professor K. Nisimura, Dr. K. Imai, and Dr. H. Shimizu for production of an efficient polarized beam, and to the staff of the AVF cyclotron at the Research Center for Nuclear Physics (RCNP) for their kind help during the experiment. This experiment was performed at the Research Center for Nuclear Physics, Osaka University, under Program Nos. 3A25, 4A03, 5A04, 6A02 and was supported in part by a Grant-in-Aid for Scientific Research, No. 442006, of the Japan Ministry of Education, Science, and Culture.

---

*Present address: Research Center for Nuclear Physics, Osaka University, Osaka, Japan.

†Present address: Institute for Physical and Chemical Research, Wako-shi, Japan.

[1]J. P. Jeukenne, A. Lejeune, and C. Mahaux, Phys. Rev. C 10, 1391 (1974).

[2]J. P. Jeukenne, A. Lejeune, and C. Mahaux, Phys. Rep. 25C, 83 (1976).

[3]J. P. Jeukenne, A. Lejeune, and C. Mahaux, Phys. Rev. C 15, 10 (1977).

[4]J. P. Jeukenne, A. Lejeune, and C. Mahaux, Phys. Rev. C 16, 80 (1977).

[5]F. A. Brieva and J. R. Rook, Nucl. Phys. A291, 299 (1977).

[6]F. A. Brieva and J. R. Rook, Nucl. Phys. A291, 377 (1977).

[7]F. A. Brieva and J. R. Rook, Nucl. Phys. A297, 206 (1978).

[8]F. A. Brieva and J. R. Rook, Nucl. Phys. A307, 493 (1978).

[9]F. A. Brieva, Phys. Lett. 76B, 533 (1978).

[10]C. W. Wong, Nucl. Phys. A91, 399 (1967).

[11]J. W. Negele, Phys. Rev. C 1, 1260 (1970).

[12]F. D. Becchetti and G. W. Greenlees, Phys. Rev. 182,

1190 (1969).
[13]E. Fabrici, S. Micheletti, M. Pignanelli, F. G. Resmini, R. DeLeo, G. D'Erasmo, A. Pantaleo, J. L. Escudié, and A. Tarrats, Phys. Rev. C 21, 830 (1980).
[14]E. Fabrici, S. Micheletti, M. Pignanelli, F. G. Resmini, R. DeLeo, G. D'Erasmo, and A. Pantaleo, Phys. Rev. C 21, 844 (1980).
[15]H. O. Meyer, P. Schwandt, G. L. Moake, and P. P. Singh, Phys. Rev. C 23, 616 (1981).
[16]A. Nadasen, P. Schwandt, P. P. Singh, W. W. Jacobs, A. D. Bacher, P. T. Debevec, M. D. Kaitchuck, and J. T. Meek, Phys. Rev. C 23, 1023 (1981).
[17]L. G. Arnold, B. C. Clark, R. L. Mercer, and P. Schwandt, Phys. Rev. C 23, 1949 (1981).
[18]H. Sakaguchi, M. Nakamura, K. Hatanaka, A. Goto, T. Noro, F. Ohtani, H. Sakamoto, and S. Kobayashi, Phys. Lett. 89B, 152 (1979).
[19]H. Sakaguchi, M. Nakamura, K. Hatanaka, T. Noro, F. Ohtani, H. Sakamoto, H. Ogawa, and S. Kobayashi, Phys. Lett. 99B, 92 (1982).
[20]T. Noro, H. Sakaguchi, M. Nakamura, K. Hatanaka, F. Ohtani, H. Sakamoto, and S. Kobayashi, Nucl. Phys. A336, 189 (1981).
[21]K. Imai, N. Tamura, and K. Nisimura, RCNP Annual Report, 1976, p. 23.
[22]M. Kondo *et al.*, Proceedings of 7th International Conference on Cyclotrons and Their Applications, Zurich, 1975 (Birkhauser, Basel, 1975), p. 95.
[23]N. Matsuoka, K. Hosono, T. Saito, A. Shimizu, and M. Kondo, RCNP Annual Report, 1976, p. 97.
[24]K. Imai, K. Hatanaka, H. Shimizu, and K. Nisimura, RCNP Annual Report, 1978, p. 154.
[25]S. Kato, K. Okada, M. Kondo, A. Shimizu, K. Hosono, T. Saito, N. Matsuoka, S. Nagamachi, K. Nisimura, N. Tamura, K. Imai, K. Egawa, M. Nakamura, T. Noro, H. Shimizu, K. Ogino, and Y. Kadota, Nucl. Instrum. Methods 169, 589 (1980).
[26]M. Q. Makino, C. N. Waddell, and R. M. Eisberg, Nucl. Instrum. Methods 60, 109 (1968).
[27]J. Raynal, Saclay, code MAGALI.
[28]G. W. Greenlees, G. J. Pyle, and Y. C. Tang, Phys. Rev. 171, 1115 (1968).
[29]L. R. B. Elton, *Nuclear Sizes* (Oxford University Press, Oxford, 1961), p. 107.
[30]B. Sinha, Phys. Lett. C20, 1 (1975).
[31]R. C. Barrett and D. F. Jackson, *Nuclear Sizes and Structure* (Clarendon, Oxford, 1977), p. 146.
[32]C. M. Perey and F. G. Perey, At. Data Nucl. Data Tables 13, 293 (1974).
[33]S. Shlomo and E. Friedman, Phys. Rev. Lett. 39, 1180 (1977).
[34]G. D. Alkhazov, S. L. Belostotsky, O. A. Domchenkov, Yu. V. Dotsenko, N. P. Kuropatkin, M. A. Schuvaev, and A. A. Vorobyov, Phys. Lett. 57B, 47 (1975).
[35]G. D. Alkhazov, T. Bauer, R. Bertini, L. Bimbot, O. Bing, A. Boudard, G. Bruge, H. Catz, A. Chaumeaux, P. Couvert, J. M. Fontaine, F. Hibou, G. J. Igo, J. C. Lugol, and M. Matoba, Nucl. Phys. A280, 365 (1977).
[36]G. C. Alkhazov, T. Bauer, R. Beurtey, A. Boudarad, G. Bruge, A. Chaumeaux, P. Couvert, G. Cvijanovich, H. H. Duhm, J. M. Fontaine, J. C. Lugol, J. Saudinos, J. Thirion, and A. A. Vorobyov, Nucl. Phys. A274, 443 (1974).
[37]G. W. Hoffmann, G. S. Blanpied, W. R. Coker, R. P. Liljestrand, N. M. Hintz, M. A. Oothoudt, T. S. Bauer, G. Igo, G. Pauletta, J. Soukup, C. A. Whitten, Jr., D. Madland, J. C. Pratt, L. Ray, J. E. Spencer, H. A. Thiessen, H. Nann, K. K. Seth, C. Glashausser, D. K. McDaniels, J. Tinsley, and P. Varghesse, Phys. Rev. Lett. 40, 1256 (1978).
[38]G. W. Hoffmann *et al.*, Phys. Lett. 76B, 383 (1978).
[39]G. W. Hoffmann *et al.*, Phys. Lett. 79B, 376 (1978).
[40]G. Igo *et al.*, Phys. Lett. 81B, 151 (1979).
[41]L. Ray, G. W. Hoffmann, G. S. Blanpied, W. R. Coker, and R. P. Liljestrand, Phys. Rev. C 18, 1757 (1978).
[42]L. Ray, W. R. Coker, and G. W. Hoffmann, Phys. Rev. C 18, 2641 (1978).
[43]G. Bertsch, J. Borysowicz, and H. McManus, Nucl. Phys. A284, 399 (1977).
[44]A. Lejeune and P. E. Hodgson, Nucl. Phys. A295, 301 (1978).
[45]F. A. Brieva, in *Microscopic Optical Potential,* edited by H. V. v. Geramb, Lecture Notes in Physics (Springer, Berlin, 1979), Vol. 89, p. 84.